Volume 1 | Number 1 | Jan 2013 | Pages 1–100

Soft Matter

www.rsc.org/softmatter

ROYAL SOCIETY OF CHEMISTRY

ROYAL SOCIETY OF CHEMISTRY

www.rsc.org/softmatter

Pulsating Electric Field Modulated Contact Line Dynamics of Immiscible Binary Systems in Narrow Confinements under Electrical Double Layer Phenomenon

Pranab Kumar Mondal,[1] *Uddipta Ghosh,*[1] *Aditya Bandopadhyay,*[2] *Debabrata DasGupta,*[1] *and Suman Chakraborty*[1,2]

[1]*Department of Mechanical Engineering, Indian Institute of Technology Kharagpur, West Bengal, India - 721302*

[2]*Advanced Technology Development Center, Indian Institute of Technology Kharagpur, West Bengal, India - 721302*

———————————————————————

Email address: suman@mech.iitkgp.ernet.in

Abstract

We investigate the interfacial electro-chemical-hydrodynamics of an incompressible immiscible binary fluid system that moves in a narrow fluidic channel under time-periodic electroosmotic effects. We apply an alternating electrical voltage that sets the binary fluids in motion along the channel, whereas the channel walls are lined with chemical patch to alter the wetting characteristics of the surface. We demonstrate that the pulsating nature of the externally applied electric field in conjunction with the wetting characteristics of the surface may lead to some fascinating behavior of the contact line motion; which, in turn, may affect the capillary filling dynamics in an intriguing manner. Our results also unveil the profound influence of two important governing factors actuating the flow, namely, the frequency and amplitude of the time periodic electric field, on the tunability of the capillary filling rate and power requirement for filling the fluids into the channel.

1. INTRODUCTION

Moving contact lines, formed at the intersection of fluid-fluid-solid interfaces, are encountered in various natural phenomena and industrial processes such as rain drops rolling down the leaves and window panes, motion of molten magma in the earth's crust, tear films on cornea and so on. From a chemical processing perspective, contact lines play a pivotal role in polymer processing, enhanced oil recovery, textile manufacturing, fabrication of photographic films to name a few. Such omnipresence of moving contact lines across disparate disciplines of science and technology has motivated researchers to interrogate systematically the underlying fundamental physics of contact line dynamics over interfacial scales through experiments, theory and molecular simulations.[1–4] More recently, with growing focus on miniaturization, controlled manipulation of small fluid volumes in *on-chip* platforms have become important for a wide gamut of applications including the design of advanced chip-cooling strategies, power generation, on-chip bio-analysis, colloidal deposition and drug delivery.[5–7] In these miniaturized platforms, the dynamics of contact line governs the overall transport in a rather profound manner and demands careful attention.[8–11]

The effect of surface wetting conditions on contact line motion and its ultimate influence on capillary filling processes along with the effect of the dynamic contact angle has been an active area of research.[12–18] Careful investigation, however, reveals that most of the concerned studies have considered a driving pressure gradient as the flow actuating mechanism over plain and patterned surfaces alike.[14,19] However, with advancements in lab-on-a-chip technology, researchers have considered the application of electric fields towards controlling contact line dynamics in microfluidic environments.[20–24] Such proposition of using electrical fields for modulating contact line dynamics holds several advantages, including integrability with on-chip circuitry and lack of moving components. However, till date, steady electric fields have primarily been considered for analyzing the interaction between substrate wettability and electrokinetic phenomena on contact line dynamics over interfacial scales.[21] On the contrary, employment of time-periodic electrical field for modulating contact line dynamics could be an interesting proposition, primarily attributed to the rich physical interplay of various spatio-temporal scales involved, as well as to its immense consequences towards arresting the adverse effects of Joule heating.[25–27]

Here we attempt to investigate the contact line dynamics of two immiscible fluids under the influences of an externally applied time periodic electric field, in presence of a uniform zeta potential. We further assume the walls of the channel to be of designed wettabilities. In order to resolve the charge distribution in the channel, we assume the presence of thick but non-overlapping electrical double layers (EDLs) adhering to the channel walls, formed as a consequence of interfacial charging phenomenon due to interaction between an ionizable fluid and a microfluidic substrate. One central result of the present analysis is that the contact line undergoes *stick-slip* (pinning-depinning) motion as the interface progresses in the channel and its velocity can be tuned intricately by altering the surface wettability and the time periodic electrokinetic phenomena, as modulated by different parameters such as the amplitude and frequency of the externally applied electric field, the zeta potential, and the characteristic EDL thickness or in other words, the Debye length (which may be manipulated by varying the solution concentration). We further demonstrate that the power required for the capillary penetration into the narrow fluidic confinement depends on the oscillatory component of the applied electric field and the surface wettability. We also highlight that the capillary filling power decreases significantly with increments in magnitudes of the time dependent part of the applied electric field and the wetting condition of the solid surface.

2. THEORITICAL MODEL

2.1 Problem description

We consider an alternating electric field- driven transport through a parallel plate capillary of height $2H$ and length L, as shown in Fig. 1. The width of the capillary is considered to be significantly larger than its height, thereby rendering the flow to be practically two dimensional.

We consider that the narrow gap between the two parallel plates is filled up with two immiscible fluids. Initially, fluid A of density ρ_1, viscosity μ_1 and permittivity ε_1 occupies an axial extent of L_1, whereas fluid B having density ρ_2, viscosity μ_2 and permittivity ε_2 occupies the remaining channel. Both the fluids in the channel are considered to have equal permittivities. The channel walls are assumed to bear a surface charge, as manifested in terms of an equivalent zeta potential, given by ζ_0. Our interest in the present study focuses on the contact line dynamics in presence of an external pulsating electric field, $\bar{E}$. We also consider that the channel walls are

chemically designed to provide a desired wettability as expressed in terms of the static contact angle θ_s. For the sake of clarity we mention that subscript 1 is used to describe the properties of liquid A and subscript 2 is used for describing the properties liquid B.
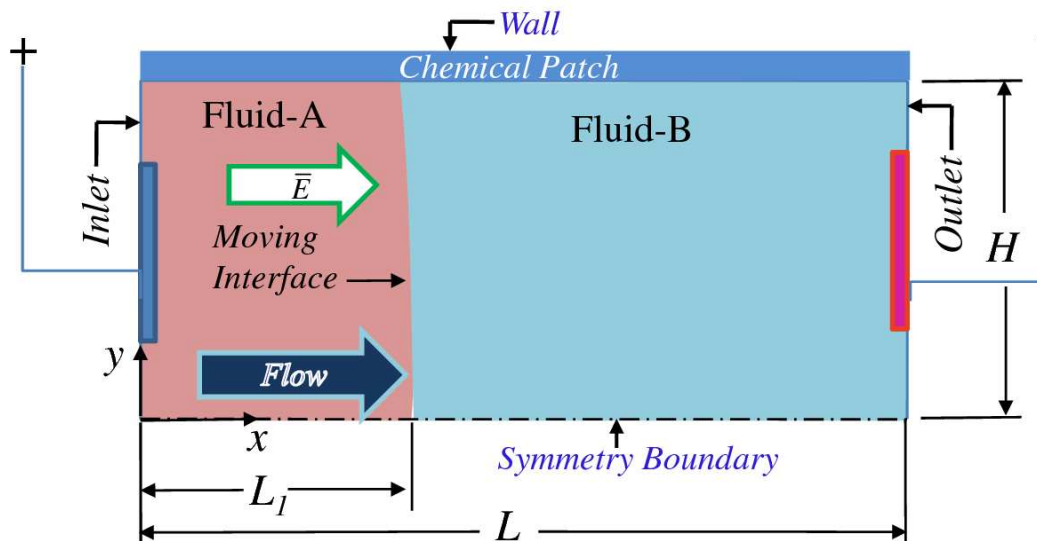

Fig. 1. (color online) Schematic of the solution domain showing the physical dimensions. The solution domain is the symmetric upper-half of the channel and the origin is placed at the center of the left end of the channel. Fluid A initially resides in the left side of the channel and fluid B initially resides in the right side of the channel. The channel wall is chemically patterned, so as to provide a designed wettability. An external pulsating axial electric field ($\bar{E}$) acts on the system, which, on interaction with an induced transverse field in the EDL, as well as with the interfacial wettability, dictates the contact line dynamics in a rather profound manner. The coordinate directions x and y are along the axial and transverse directions which run along the channel length and channel height, respectively.

2.2. Mathematical formulation

2.2.1. Phase field model

We use diffuse interface based phase field model [14,21,28–34] in addressing the fluid motion in the capillary. In the phase field method, two immiscible fluids in a binary system can be described by an order parameter ϕ, which describes the state of the system owing to the composition of the fluid at any instant, is defined in terms of the normalized phase concentrations of the respective phases. In the presents study, the order parameter is defined in the following way: $\phi = (n_A - n_B)/(n_A + n_B)$, where, n_A and n_B denotes the number of molecules of the displacing phase fluid (fluid A, $\phi = 1$) and displaced phase fluid (fluid B, $\phi = -1$)

respectively. The value of the order parameter smoothly transits across the interface of the two phases. The Ginzburg-Landau free energy functional of the binary fluid system can be expressed as the function of the order parameter. In our present analysis, we express the free energy functional in the following way:[14,21,31,35–39]

$$F = \int_{\forall} \left\{ f(\phi) + \frac{1}{2}\sigma\xi|\nabla\phi|^2 \right\} dV \tag{1}$$

The first term of Eq. (1) is the bulk energy density, which is responsible for the immiscibility of the fluids, and the second term is the free energy excess of the interface which accounts for the presence of diffuse interface of finite thickness separating the bulk phases. We may cast the first term in Eq. (1) in the form of a double well potential as given below:[40,41]

$$f(\phi) = \frac{\sigma}{4\xi}\left(1 - \phi^2\right)^2 \tag{2}$$

where the two minima $(\phi = \pm 1)$ correspond to the two stable phases A and B respectively.

In equations (1–2), σ is the surface energy per unit area. The parameter ξ, which denotes the diffuse interface thickness, is of the order of $10^{-9} - 10^{-8}$ m.[33,36] The chemical potential is defined as the variation of free energy with respect to the phase concentration function ϕ, and is given by:

$$\mu = \frac{\delta F}{\delta\phi} = f'(\phi) - \sigma\xi\nabla^2\phi \tag{3}$$

The distribution of the order parameter in equilibrium condition is obtained by equating the chemical potential to a constant.

2.2.2. Cahn-Hilliard model coupled with time periodic electro-hydrodynamics

In this Sub-section, we attempt to outline the governing transport equations for the present problem (for a schematic depiction, along with the boundary conditions, see Fig. 2). First, we describe the equations that describe the phase-field evolution, and then we discuss about the coupling between phase-field dynamics and time periodic electro-mechanics. The evolution of the order parameter, ϕ, is governed by the Cahn-Hilliard (CH) equation:[14,21,40–42]

$$\frac{\partial\phi}{\partial t} + \mathbf{u}\cdot\nabla\phi = \nabla\cdot(M\nabla\mu) \tag{4}$$

In the phase field model, one can, therefore, find the variation of the order parameter ϕ with time (temporal variation) as well as the variation of ϕ owing to the presence of either an induced or an imposed velocity field (advection), in effect allows to cast the CH equation in the total or material time derivative form as given by equation (4). It is to be mentioned here that $M\,(>0)$ is a phenomenological constant, which controls the diffusion across the interface and is termed as mobility parameter. The boundary conditions for equation (4) are given by:

$$\nabla\mu\cdot\mathbf{n} = 0 \tag{5a}$$

$$\mathbf{n}\cdot\nabla\phi = -\tan\left(\frac{\pi}{2}-\theta_s\right)\left|\nabla\phi-(\mathbf{n}\cdot\nabla\phi)\mathbf{n}\right| \tag{5b}$$

where $\mathbf{n}$ is the unit normal vector pointing outward from the solid surface.

Eq. 5(a) indicates zero flux across the surface, while Eq. 5(b) locally adjusts the order parameter profile near the boundary. The boundary condition given in Eq. 5(b) ensures that the contact angle θ_s remains at its specified value at the boundary and the order parameter remains approximately constant along the tangent to the interface.[42]

2.2.3. Electrical potential distribution

We next outline the equations governing the charge distribution in the channel. We assume that the channel substrates intrinsically develop some surface charge (for instance, due to ion adsorption), leading to EDL phenomenon.[43] This leads to a distribution of induced interfacial potential ψ, as governed by the Poisson-Boltzmann equation for a $z:z$ symmetric electrolyte [44].

$$\nabla\cdot[\varepsilon\nabla\psi] = 2\rho_0\sinh\left(\frac{ze\psi}{kT}\right) \tag{6}$$

In Eq. (6), ε is the permittivity of the fluid and ρ_0 is the reference charge density in the bulk, e is the protonic charge, k is the Boltzmann constant and T is the absolute temperature. In compliance to the diffuse interface approach considered in the present analysis, the permittivity in equation (6), can be expressed as:[45]

$$\varepsilon = \varepsilon_1\left(\frac{1+\phi}{2}\right) + \varepsilon_2\left(\frac{1-\phi}{2}\right) \tag{7}$$

We define the boundary conditions for equation (6) as given by: $\psi(x,-H)=\psi(x,H)=\zeta_0$. The net electric charge density, ρ_e, for an symmetric electrolyte can be described by the Boltzmann distribution:[46,47]

$$\rho_e = -2\rho_0 \sinh\left(ze\psi / kT\right). \tag{8}$$

It is important to mention here that in addition to the induced electrical field described as above, an externally applied pulsating axial electric field ($\psi*$) also acts on the fluid system. The later satisfies the Laplace equation:[46,48]

$$\nabla\cdot\left[\varepsilon\nabla\psi*\right]=0 \tag{9}$$

Eq. (9) satisfies the boundary conditions: $\psi*(0,y)=V_0[1+a\sin(\omega t)]$; $\psi*(L,y)=0$; $\nabla\psi*\cdot\mathbf{n}=0$ at the walls. It is also important to mention that in the present analysis, the applied electric field is time periodic in nature and hence is likely to give rise to a time varying flow velocity. This, in turn, is likely to make the charge distribution in the channel time dependent. However, a simple non-dimensionalization of the Nernst-Planck equation (equation governing advection-diffusion transport of the ionic species) depicts that the relative contribution of the advective strength of the ionic species as compared to diffusive strength is reflected by the ionic Peclet number, which can be expressed as $Pe = \dfrac{u_{ref}L_{ref}}{D}$, where u_{ref} is the reference velocity, L_{ref} is the reference length scale and D is the ionic diffusivity. For electro-osmotic flows, typical velocity scale is in the tune of $u_{ref} \sim \dfrac{\varepsilon\zeta_0 E}{\eta}$ (E is the applied axial electric field and η is the fluid viscosity), whereas the typical length scale is given by the channel height H.[44] Taking water as the medium ($\varepsilon \sim 6\times10^{-10}, \eta \sim 10^{-3}$), for an axial electric field of $E \sim 10^4$ V/m and for $\zeta_0 \sim 100$ mV, one gets $u_{ref} \sim 6\times10^{-4} m/s$. Now, with a channel height of $H \sim 100$ nm and $D \sim 10^{-8} - 10^{-9}$ m²/s (typical values of ionic diffusivity),[49] the Peclet number comes out to in the tune of Pe $\sim 0.01 - 0.001$. This simple calculation indicates that the contribution of the advection on the space distribution of ionic charges can be safely neglected in the present analysis. Quite intuitively, it is these advection effects which introduce the time dependency of charge distribution in the channel. Since we have already shown that the advection of ionic species plays a negligible role as compared to diffusion and migration, we can go one step further and use the standard Poisson-

Boltzmann equation to deduce the ionic concentrations and the potential, as has been done in equation (6). However, for the sake of completeness we additionally mention the various time scales involved in the formation of EDL and charge dynamics. A much detailed account of these time scales can be found in the work of Bazant et al;[50] here we only mention briefly the physical implications of the different time scales involved. The shortest time scale is the Debye time scale or the charge relaxation time scale, which is expressed as, $\tau_D \sim \dfrac{\kappa^2}{D}$ (where κ is the Debye length) and denotes the time scale of individual charge relaxation within the EDL. The second time scale, known as the RC time scale, is expressed as, $\tau_{RC} \sim \dfrac{\kappa H}{D}$, which signifies the typical time scale for the EDL to reach equilibrium thickness. A physical basis of the introduction of this time scale lies in the fact that the combination of EDL and the bulk essentially acts as a series RC circuit, when a potential is applied at the fluid-solid interface. Accordingly, the RC time scale is basically the typical time taken by the EDL to get fully charged.[51] The third and the longest time scale is the bulk diffusion time scale, given by $\tau_B \sim \dfrac{H^2}{D}$,[51,52] where D and H are defined earlier.

This time scale basically indicates the time taken by the ions to diffuse to nullify any concentration difference in the channel. The channel height H ($\sim$ 100 nm) along with the usual diffusivity of ions ($D \sim 10^{-8} - 10^{-9}$ m^2/s) makes the diffusive time scale to be in the tune of $\sim 10^{-5} - 10^{-6}$ s. Clearly the two important time scales, which directly dictate the charge distribution, are first two scales. In the present study, the EDL thickness has been taken to be in the tune of $\kappa \sim 10\,nm$. Therefore, for the present study we have, $\tau_D \sim 10^{-7} - 10^{-8}\,s$ and $\tau_{RC} \sim 10^{-6} - 10^{-7}\,s$ (with D values taken same as in the previous calculation). For the time varying axial electric field, the frequencies have been taken to be in the tune of $\bar{\omega} \sim 1 - 10\,kHz$, involving typical time scales of 10^{-4} s, which, therefore, are much larger than the charge relaxation and RC time scales in the channel. This again demonstrates that the EDL is in quasi-equilibrium as compared to the axial time varying electric field, as attributable to a much faster charge relaxation process. Therefore, one can safely apply the Boltzmann distribution in equation (6) and (8) to obtain the potential and the charge distribution.

2.2.4. Cahn-Hilliard-Navier-Stokes equation

The governing equations for fluid flow can be described by the modified Cahn-Hilliard-Navier-Stokes equation (Eq. 10.a), coupled with the continuity equation (10.b), with additional terms accounting for electro-hydrodynamic interactions:

$$\rho\left(\frac{\partial \mathbf{u}}{\partial t}+\mathbf{u}\cdot\nabla\mathbf{u}\right)=-\nabla p+\nabla\cdot\left[\eta\left(\nabla\mathbf{u}+\nabla\mathbf{u}^{T}\right)\right]-\rho_{e}\nabla\psi*+\mu\nabla\phi+\frac{1}{2}\nabla\varepsilon\left(\mathbf{E}.\mathbf{E}\right)+\nabla\left(\rho\frac{\partial\varepsilon}{\partial\rho}\mathbf{E}.\mathbf{E}\right)\text{(10.a)}$$

$$\nabla\cdot\mathbf{u}=0 \tag{10.b}$$

where u and v are the velocity components in the x and y direction respectively. We consider the density ρ and viscosity η to be explicit functions of the order parameter as governed by the relative phase fractions:[14,33]

$$\rho=\rho_{1}\left(\frac{1+\phi}{2}\right)+\rho_{2}\left(\frac{1-\phi}{2}\right) \tag{11.a}$$

$$\eta=\eta_{1}\left(\frac{1+\phi}{2}\right)+\eta_{2}\left(\frac{1-\phi}{2}\right) \tag{11.b}$$

It is important to mention here that the penultimate terms in Eq. (10.a) arise due to the spatial variation in the permittivity, whereas the last terms in these equations are consequences of an electrostriction force that originates when permittivity becomes a function of density. Further, in Eq.10.a, $\mathbf{E}$ is the total electric field, combining the induced EDL field as well as the applied axial electric field. In the diffuse interface method, a thin but numerically resolvable region of transition between two different values of order parameters exists through which most of the phase variation takes place, essentially results in a large diffusive flux. These large diffusive fluxes distort the velocity field, which eventually leads to the local change in the topology of the interface. The local change in the interface curvature multiplied by the surface tension gives rise to an additional term, $\mu\nabla\phi$ in the momentum balance equation as given in the right hand side of equation (10.a).

We apply the standard no-slip and no-penetration boundary conditions at the channel wall, so that $u = v = 0$. Further, we take inlet (p_{in}) and outlet (p_{out}) gauge pressures to be zero and the initial velocity in the domain $\mathbf{v}\left(x,y,t=0\right)=0 \ \forall \ x,y$.

2.2.5. Non-dimensional equations

Having established the set of governing transport equations and the necessary boundary conditions, next we proceed to non-dimensionalize the aforementioned equations. Towards this,

we adopt the following non-dimensionalization scheme: $\bar{\psi}^* = \psi^*/(V_0\xi/L)$; $\bar{u} = u/u_0$;

$\bar{v} = v/u_0$; $\bar{x}, \bar{y} = x/\xi, y/\xi$; $\bar{\psi} = ze\psi/kT$; $\bar{\eta} = \eta/\eta_{ref}$; $\bar{\rho} = \rho/\rho_{ref}$; $\bar{\varepsilon} = \varepsilon/\varepsilon_{ref}$; $\bar{p} = p/p_{ref}$;

$\bar{\omega} = \omega t_{ref}$ and $\bar{t} = t/t_{ref}$, where $p_0 = \eta_{ref}u_0/\xi$; $t_{ref} = \xi/u_0$ and $u_0 = \dfrac{\varepsilon_{ref}kTV_0}{ze\eta_{ref}L}$. The chemical

potential is non-dimensionalized as: $\bar{\mu} = \mu/(\sigma/\xi)$. Enforcing the scheme of non-dimensionalization mentioned above and considering the two fluids to be of identical densities and permittivities, we arrive at the final dimensionless equations in the form:

$$\frac{\partial\bar{\phi}}{\partial\bar{t}} + \bar{u}\cdot\nabla\bar{\phi} = \frac{1}{Pe}\nabla\cdot(\bar{M}\nabla\bar{\mu}) \tag{12}$$

$$\nabla\cdot[\bar{\varepsilon}\nabla\bar{\psi}] = \bar{\lambda}^2\sinh(\bar{\psi}) \tag{13}$$

$$\nabla\cdot[\bar{\varepsilon}\nabla\bar{\psi}^*] = 0 \tag{14}$$

$$Re\,\bar{\rho}\left(\frac{\partial\bar{u}}{\partial\bar{t}} + \bar{u}\cdot\nabla\bar{u}\right) = -\nabla\bar{p} + \nabla\cdot\left[\bar{\eta}\left(\nabla\bar{u} + \nabla\bar{u}^T\right)\right] - \bar{\lambda}^2\sinh(\bar{\psi})\nabla\bar{\psi}^* + \frac{1}{Ca}\bar{\mu}\nabla\bar{\phi} \tag{15}$$

$$\nabla\cdot\bar{u} = 0 \tag{16}$$

It is important to note that in the non-dimensionalization scheme, one can use either of fluid properties to be the reference values of the different fluid properties (like viscosity and density) to define the two phase flow configuration. In the present study, we have considered the properties of fluid A as the reference properties. Various dimensionless parameters appearing as above may be defined as: Peclet number $Pe = u_0\xi^2/M_c\sigma$, Capillary number $Ca = u_0\eta_{ref}/\sigma$, and Reynolds number $Re = \rho_{ref}u_0\xi/\eta_{ref}$. In Eq. (12), we define $\bar{M}$ as: $\bar{M} = M/M_c$ where M_c is defined following reported MD simulation studies[15] as: $M_c = Cl^4/\sqrt{\tilde{m}\varepsilon_e}$; l and ε_e being the length scale and energy scale respectively in the Lennard-Jonnes potential for fluid molecules and $\tilde{m}$ being the molecular mass of fluid, and C is a constant (given by 0.023). We consider the value of dimensionless Mobility parameter $\bar{M} = 1$ for all of our numerical simulations The term λ in equation (13), which is called the inverse of Debye length, can be expressed as: $\lambda = (2\rho_0 ze/\varepsilon_{ref}kT)^{1/2}$ and $\bar{\lambda} = \lambda\xi$.
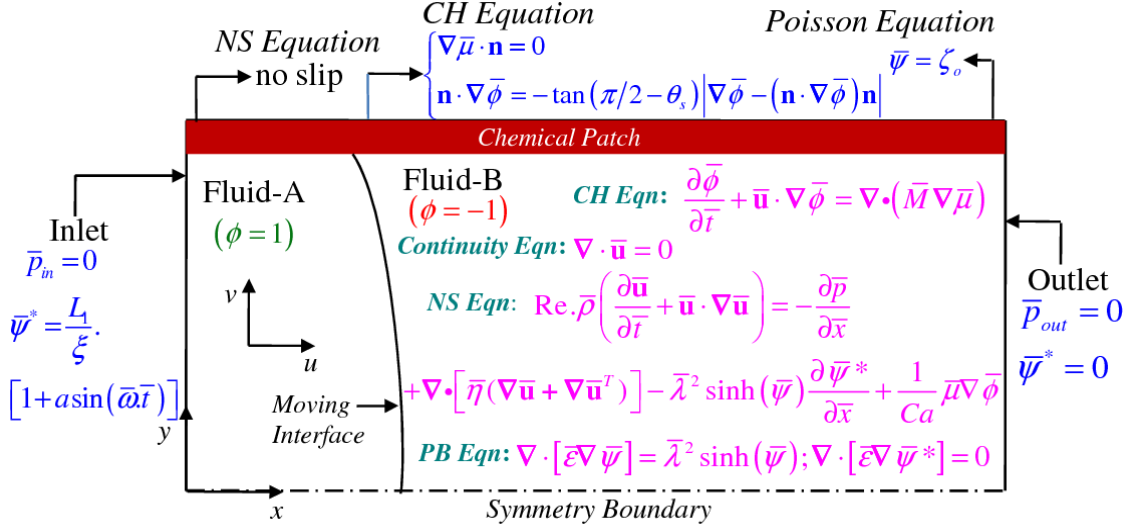
Fig. 2. (color online) Schematic of the solution domain showing the govering transport equations and the apprppriate boundary conditions. The channel walls bear spatially uniform zeta potential (ζ_0). The channel wall is chemically patched, characterized by predifined contact angle θ_s. There is an externally applied time periodic electric field, which actuates the fluid motion.

2.3. Capillary penetration power

In this Sub-section, we make an effort to estimate the power required for the capillary penetration. In order to do so, we first calculate the number density of both positive and negative ions present in the fluids, which is given by:

$$\text{Positive charge density, } n_+ = n_0 \exp(-\frac{ze\psi}{kT}) \tag{17}$$

$$\text{Negative charge density, } n_- = n_0 \exp(\frac{ze\bar{\psi}}{kT}) \tag{18}$$

where n_0 represents the bulk number density of the ions. The above can be expressed in the following dimensionless forms:

$$\text{Dimensionless positive charge density, } \bar{n}_+ = \frac{n_+}{n_0} = \exp(-\bar{\psi}) \tag{19}$$

$$\text{Dimensionless negative charge density, } \bar{n}_- = \frac{n_-}{n_0} = \exp(\bar{\psi}) \tag{20}$$

Next, we write the expresions for the ionic current densities. The dimensional form of the current density of the positive ions can be written as:

$$j_+ = n_+ u_+ ze \qquad (21)$$

where the term $u_+ = \left(u_f + \dfrac{zeE}{f} \right)$ represents the drift velocity, which comprises the velocity of

the fluid u_f and the velocity of the positive ions due to the externally applied electric field $\dfrac{zeE}{f}$.

The parameter f represents the ionic friction factor. It is important to mention here that the typical value of friction factor we consider in the present study is $f \sim 10^{-12}$.[50] Accordingly, we arrive at the following dimensionless form of the current density of the positive ions:

$$\overline{j}_+ = \frac{j_+}{j_{ref}} = \overline{n}_+ \left(\overline{u}_f + \frac{zeE_{ref}}{f u_{ref}} \overline{E} \right) \qquad (22)$$

where $j_{ref} = zen_0 u_{ref}$, $u_{ref} = u_0$ and $E_{ref} = V_0/L$ (please refer to Section 5 of mathematical formulation part for the respective reference parameters). In a similary way, the dimensionless form of the current density of the negative ions can be expresses as:

$$\overline{j}_- = \frac{j_-}{j_{ref}} = \overline{n}_- \left(\overline{u}_f - \frac{zeE_{ref}}{f u_{ref}} \overline{E} \right) \qquad (23)$$

The power density required to drag the binary fluids along the capillary is given by:

$$P(\overline{x}, \overline{y}, \overline{t}) = JE = (j_+ + j_-)E = j_{ref} E_{ref} (\overline{j}_+ + \overline{j}_-) \overline{E} \qquad (24)$$

We non-dimensionalize the power density with $\overline{P} \rightarrow P / j_{ref} E_{ref}$. The net dimensionless power, $\tilde{P}$, given by:

$$\tilde{P}(\overline{x}, \overline{t}) = \int_0^{\overline{H}} \overline{P}(\overline{x}, \overline{y}, \overline{t}) d\overline{y} \qquad (24.a)$$

where the net dimensionless power is normalized as $\widehat{P} \rightarrow \tilde{P} / j_{ref} E_{ref} \xi$. The total space average power is given by:

13

$$P_{avg}\left(\overline{t}\right)=\frac{1}{\overline{L}}\int_{0}^{\overline{L}}\widehat{P}(\overline{x},\overline{t})d\overline{x} \tag{25}$$

Based on the expresion of the average power as given in Eq. (25), we calculate the dimensionless rms power P_{rms} , given as:

$$P_{rms}=\sqrt{\frac{1}{T}\int_{0}^{T}[P_{avg}(\overline{t})]^{2}\,d\overline{t}} \tag{27}$$

2.4 Numerical implementation and model validation

We have used the commercial software package COMSOL® in order to solve the relevant governing equations. We have specified tolerance levels of 10^{-6} for all the numerical simulations. We have used PARDISO solver and generalized-α scheme for temporal discretization. We have validated the numerical results extensively, by using the results reported by Wang et al,[14] whose model and numerical framework are in turn benchmarked against molecular dynamic (MD) simulation.[15] However, for the sake of completeness, in figure below, we show the variation of the contact line velocity with distance along the channel. The results show extremely good agreement with those reported by Wang et al.[14]
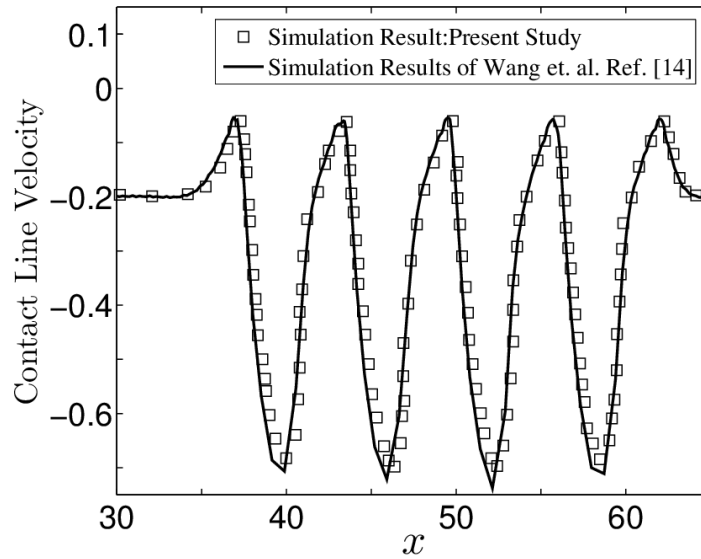

Fig. 4. Model benchmarking. Contact line velocity shown as a function of distance along the capillary. The simulations results using the present model are represented by the solid lines and

the square markers are used to represent the results reported by Wang et al.[14] The results of the present numerical framework show fairly accurate match with the reported numerical results.

The excellent match of the results predicted using the present model with those reported in the literature vouch for the correctness of the model used in the present study.

3. RESULTS AND DISCUSSIONS

As mentioned earlier, the main aim of the present study is to show the evolution of the interface over a surface of constant wettability (as specified through the respective contact angle) along with the dynamics of the contact line, for the given applied external field and interfacial (zeta) potential. Towards this, we note that the dynamics of the contact line as well as the interface is strongly dictated by the following parameters: (i) characteristic length scale EDL (λ), (ii) zeta potential (ζ_0), (iii) the contact angle at the fluid-fluid-solid interface (θ_s), (iv) frequency of actuation ($\bar{\omega}$), (v) amplitude of actuation (a), and (vi) the property ratios, for example density ratio, viscosity ratio etc. In order to isolate the other effects, we take all the relevant properties of the two fluids to be the same, as considered in a number of previous studies which means $\rho_1 = \rho_2$; $\eta_1 = \eta_2$; $\varepsilon_1 = \varepsilon_2$.[14,21,28,33] Here, it is worth mentioning that, the effects of fluid properties (like viscosity, density permittivity etc) on the motion of the contact line might be hugely non-intuitive and non-trivial and should be addressed in a separate study. Thus, in essence, here we primarily focus on bringing out the essential features of the motion of the contact line and the interface, when parameters like frequency ($\bar{\omega}$), the contact angle (θ_s) and the amplitude indicator (a) are varied. We mention the values of all the relevant parameters appearing in the present study, which remain unchanged throughout: $\text{Re} = 0.01$, $\text{Pe} = 0.2$, $\text{Ca} = 0.08$, $\zeta_0 = -4$ and $\lambda = 0.2$. We further note that from here onwards we will drop the bar signs from the variable symbols used to represent non-dimensional quantities for the convenience of presentation.

3.1. Contact line velocity (v_{cl}): Effect of frequency ($\bar{\omega}$) and amplitude (a) of the time periodic electric field for $\theta_s = 45^0$
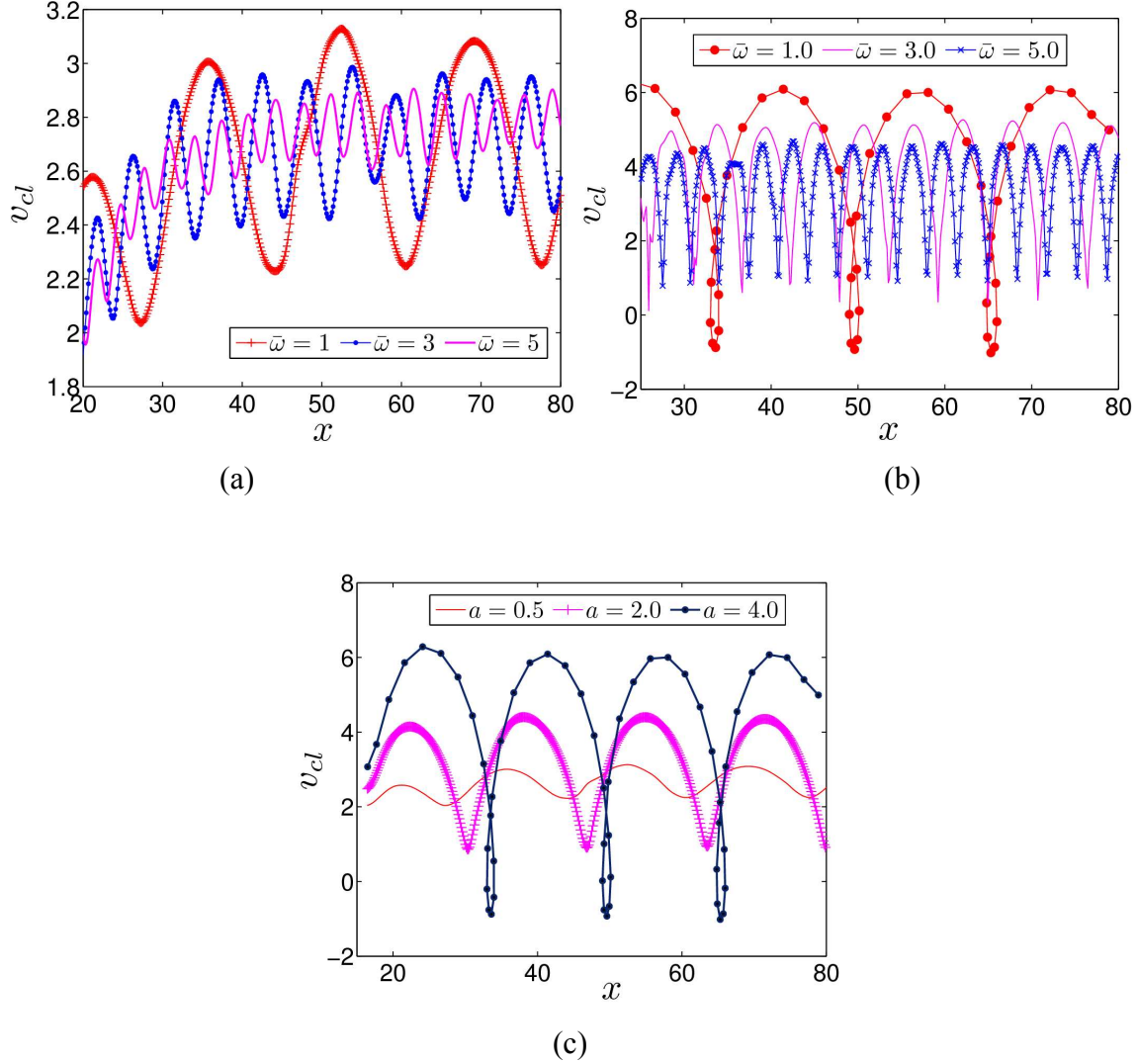
(a)

(b)

(c)

Fig. 3. (Color online) Contact line velocity V_{cl} vs. x for $\theta_s = 45^0$ (a) a =0.5, $\bar{\omega}$=1,3,5 (b) a =4.0, $\bar{\omega}$=1,3,5 and (c) $\bar{\omega}$ =1 and for different a = 0.5, 2, 4. The time varying (sinusodially) part of the applied electric field results in a time varying velocity, periodic in nature. For the given static contact angle $\theta_s = 45^0$, the contact line receding is seen only for the case of low frequency ($\bar{\omega}$ =1) at a =0.5 and for high amplitude (a = 4) at $\bar{\omega}$ =1 of the applied time periodic electric field.

We begin our discussion with figures 3(a) – 3(c), where we plot the variation of contact line velocity (denoted by V_{cl}) as a function of the distance along the channel (x). The values of the relevant parameters have been mentioned in the caption. We first concentrate on figure 3(a), where we plot V_{cl} with x for a low value of a = 0.5, corresponding to $\theta_s = 45^0$. Quite intuitively, the presence of a time varying (sinusoidal) component of the actuating electric field results in a time varying velocity, periodic in nature, although, not strictly following a sinusoidal variation as

16

attributable to the non-linearities involved in the governing two phase transport equations (12 - 17) and the boundary conditions. It is also expected that the oscillations in the velocity will be more pronounced for lower frequencies, as evident from the present figure, where the oscillations are most prominent for $\bar{\omega} = 1$ and least prominent for $\bar{\omega} = 5$. This can be attributed to the fact that for high frequencies the capillary gets less time to adjust to the rapid changes occurring in the direction of the external forcing, which is manifested in terms of a less oscillating contact line velocity. This trend, interestingly, is analogous to the contact line dynamics obtained on patterned substrates with a designed spatial frequency, as reported by Wang et al[14] and Mondal et al.[21] In those cases as well, the oscillations in the velocity becomes much smaller when the spatial frequency of the wettability patterning becomes high. Next, we focus on Fig. 3(b), where the same quantities are plotted, albeit for the case of $a = 4$. The most interesting point to note from the present figure is the phenomenon of contact line receding, which is indicated by the negative values of V_{cl}. This happens for the presence of a strong time varying component of the applied axial electric field, which changes in direction periodically, forcing the capillary to retract in the opposite direction in the process. Note that for the case of $a = 0.5$, this opposite forcing is still present; however, it only becomes strong enough to make the capillary recede, when the value of a typically exceeds a threshold value depending on the frequency. Again we note that the receding phenomenon is absent for higher frequencies, for example, for $\bar{\omega} = 5$, as attributable to the fact that for such high forcing frequencies, the direction of the applied field changes very rapidly and hence the contact line does not get enough time to recede. Therefore, in essence, we can intricately control the receding of the contact line through manipulating the frequency of the external electric field and the amplitude of the same. Following the above discussion it becomes quite clear that as we make the frequency higher, higher values of a are needed, in an effort to make the contact line recede. In an effort to demonstrate the effect of a on the contact line dynamics more clearly, we move on to figure 3(c), where the same quantities are plotted for $\bar{\omega} = 1$ and $a = 0.5, 2$ and 4. It is interesting to note that even for a as high as 2, the contact line receding is not able to take place, which underlines the influence of inertia of the capillary. As depicted in the previous figures, receding of the contact line happens for $a = 4$. At this point it worth mentioning that in the present figure we have taken the contact angle to be 45^0, which somewhat aids the forward motion of the filling fluid (fluid-A)

17

and thus acts against the phenomenon of contact line receding. In the forthcoming figures we show that the contact line receding phenomenon can be altered by altering the contact angle.

3.2. Implication of the time periodic electric field on the capillary filling dynamics

In the effort to capture the complete motion of the binary fluid system through the channel, we plot the interface position at different times as the capillary progresses along the channel for $\bar{\omega} = 1$, $a = 4$ and $\theta = 45^0$, as shown in figure 4. The present figure shows that not only the contact line, but the whole fluid front also recedes as the direction of the forcing changes, as indicated by the overlapped interface contours (crowding zone, indicated by A,B,C) shown in the present figure. It can be observed from the figure under consideration that the receding is more prominent for the central position of the interface as compared to the contact line. In figure 5(a), we plot the position of the interface centerline (x) with time (t_f) for a =4 and different forcing frequencies: ω = 1, 2, 3 and 5. It is very clearly observed that the interface witnesses a receding motion for lower frequency as does the contact line, as depicted in the previous figures (see figures 3 and 4) as well. However, similar to the motion of the contact line, this receding ceases to exist when the frequency is increased. Justification for this phenomenon has already been provided in the context of the previous figures (Fig. 3).
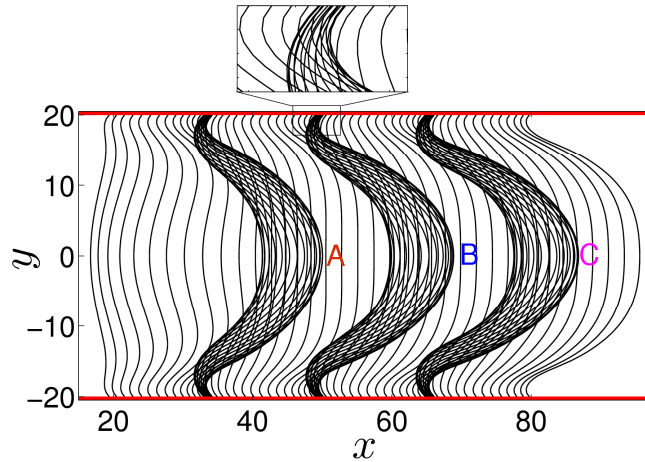

Fig. 4. (Color online) Interface evolution with interface position for $\theta_s = 45^0$, a =4, $\bar{\omega} = 1$. The surface wetting condition corresponding to value of static contact angle $\theta_s = 45^0$ allow the whole fluid front to recede as the direction of the forcing changes, as seen by the overlapped interface contours (crowding zone, indicated by A,B,C).
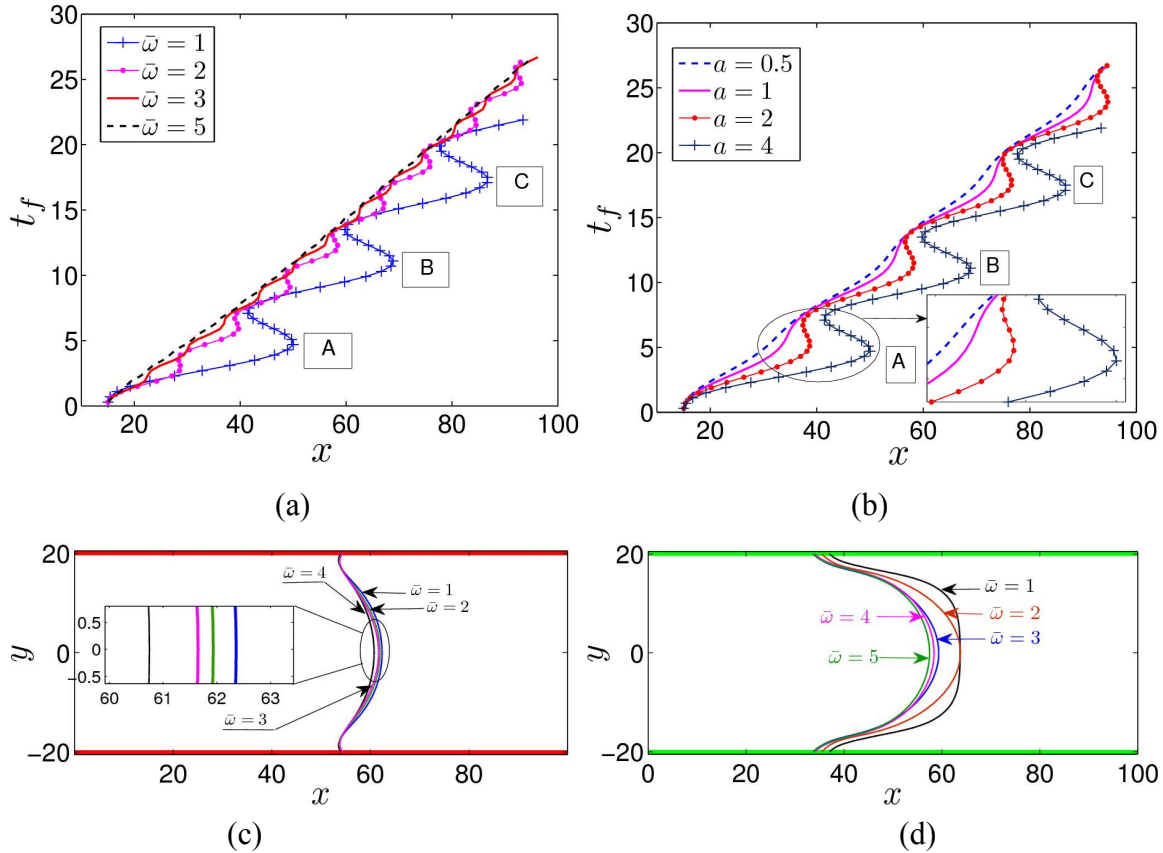
18

(a)

(b)

(c)

(d)

Fig.5. (Color online) (a) Time (t_f) vs Capillary filling distance (x), for $\zeta_0 = -4$, $\lambda = 0.2$, $\theta_s=45^0$ (a) $a =4.0$ and $\bar\omega=1,2,3,5$. (b) $\bar\omega=1$ and $a =0.5,1,2,4$. (c) Interface position at a fixed time t=150 for $\zeta_0 = -4$, $\lambda = 0.2$, $a=2$, $\theta_s = 45^0$ for different $\bar\omega=1,2,3,4$. (d) Interface position at a fixed time t=120 for $\zeta_0 = -4$, $\lambda = 0.2$, $a=2$, $\theta_s =135^0$ for different $\bar\omega=1,2,3,4,5$.

The present figure (Fig. 5a) is also in concurrence with the fact that the velocity fluctuations are small for high frequencies, as discussed in the context of figure 3, since the x versus t_f plot turns out to be an almost linear for higher frequencies ($\omega = 3$ and 5). Moving on to figure 5(b), where t_f with x has been plotted for the centerline of the interface for $\bar\omega=1$ and different values of $a = 0.5, 1, 2$ and 4, we note from this figure that the centerline of the interface recedes (see inset of Fig. 5b, where reversal of the interface is clearly observed for a=2 and $\bar\omega=1$ as shown by a line with marker 'o') even when $a = 2$ and $\bar\omega=1$, whereas for the motion of the contact line no receding occurs (see figure 3c) for the same set of parameters. This, in essence depicts a very interesting phenomenon, i.e., for relatively high values of the amplitude of the time periodic part of the applied electric field, the central part of the interface recedes, where as the contact line

does not, for the given contact angle. This, in turn, indicates that for this mismatch of motion between different parts of the interface, the interface gets deformed unusually under the application of time varying actuating axial electric field, as reflected in Figs. 5(c)-(d). Figure 5(c) shows the interface position for different values of the $\bar{\omega}$=1,2,3,4 obtained at t=150, specific to the case of $\theta_s = 45^0$, whereas in Fig. 5(d), we show the interface position for different $\bar{\omega} = 1, 2, 3, 4, 5$ obtained at $\theta_s = 135^0$. One can clearly see how the evolution of the interface changes with the time variyng part of the axially appled electric field, with other common parameters remaining unaltered. While the central part of the interface receds with the alterations in the frequency of the appied electric field; the contact line remains almost intact in its position. The gross outcome of this, however, is the drastic change in the filling dynamics as aptly reflected by the capillary penetration time, which one can find from Fig. 5(a).

3.3. Contact line velocity (v_{cl}): Effect of frequency ($\bar{\omega}$) and amplitude (a) of the time periodic electric field for $\theta_s = 135^0$

In section A, we have demonstrated the variation of contact line velocity for different values of amplitudes and frequencies of the externally applied pulsating electric field and discussed how the interfacial dynamics of contact line motion gets affected by the combined consequences of the interfacial electrochemistry and wettability, corresponding to $\theta_s = 45^0$. Here, we will see the same variation obtained at different wetting characteristics of the solid surface corresponding to $\theta_s = 135^0$, while all other simulation parameters used being mentioned in the figure captions.
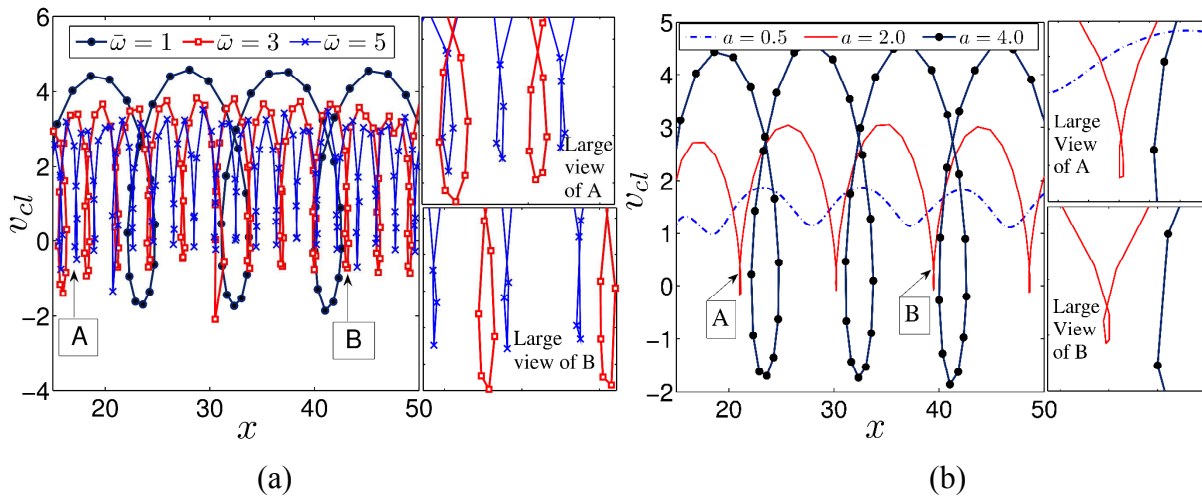

(a)   (b)

Fig. 6. (color online) Contact line velocity V_{cl} *vs.* *x* for θ = 135^0 (a) *a* =4, $\bar{\omega}$=1,3,5 and (b) $\bar{\omega}$ =1and for different *a* =0.5, 2,4 . For relatively higher value of amplitude *a* =4, the contact line receding is seen for all the values of frequency considered, while contact line receding is absent for lower value of amplitude and at $\bar{\omega}$ =1.

Figures 6(a)-(b) demonstrate the contact line velocity (V_{cl}) as a function of position, for $\theta_s = 135^0$. Figure 6(a) depicts the contact line velocity variation with *x*, for different frequencies $\bar{\omega} = 1,3$ and 5 and *a* = 4. We observe that for a contact angle of $\theta_s = 135^0$, the receding of the contact line is more prominent, even when the frequencies are high, e.g. $\bar{\omega} = 5$, for which we notice a very weak receding of the contact line. This is actually quite intuitive, since the high value of the contact angle tries to restrict the motion of the contact line and hence when aided by the action of an opposing force, the contact line starts receding. Figure 6(b) shows the variation in the same quantities for a given frequency ($\bar{\omega}$=1) and different values of *a* =0.5, 2 and 4. Quite interestingly, even for a value of *a* = 2 we still observe contact line receding, whereas the same is absent for *a* = 0.5. This is in contrast with the previous figures 3(c), where we showed that the receding does not happen when *a* = 2, with $\theta_s = 45^0$. We have already provided an explanation for this phenomenon, which indicates that for high values of contact angles, the receding happens even when the magnitude of the time periodic component of the axial electric field is not too high.
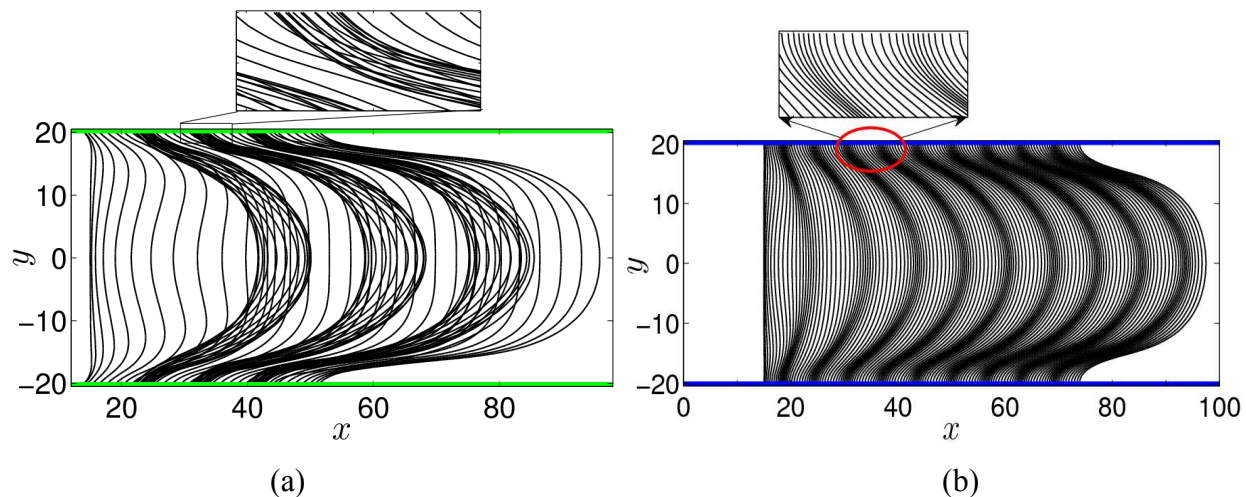

Fig. 7. (color online) Interfacial evolution (a) for $\theta_s = 135^0$, *a* = 4, $\bar{\omega}$=1 and (b) for $\theta_s = 90^0$, *a* = 2, $\bar{\omega}$=1. The surface wettability corresponding to value of static contact angle $\theta_s = 135^0$ allows the central part of the interface to get more deformed causing contact line to recede. On the other

hand, contact line receding phenomena is absent for contact angle $\theta_s = 90^0$ for a small frequency and at a relatively larger amplitude of the imposed oscillation of the time periodic electric field.

3.4. Implication of the time periodic electric field and surface wettability on the interfacial evolution.

We further demonstrate the evolution of the interface as it progresses along the channel for $\bar{\omega} = 1$ and $a = 4$, as depicted in figure 7(a). The receding of the contact line is again clearly visible from the overlapping of the interface. Another interesting point to note from the present figure is that shape of the interface is highly deformed, since the central part of the interface tries to move towards the channel end, whereas, the contact line tends to move slowly as attributable to the high value of the contact angle. This deformation is clearly more pronounced than the cases of favorable contact angle of $\theta_s = 45^0$. Figure 7(b) shows the time sequence plot of the interface profile for $\theta_s = 90^0$ obtained at a relatively higher value of amplitude of the applied electric field $a = 2$ and lower value of frequency $\bar{\omega} = 1$. One can clearly see that the contact line receding phenomena is not present even at high value of amplitude when the wetting characteristics of the surface do not have any preference towards either of the fluids have been considered in the present study.

The motion of the central part of the interface is revealed in figure 8(a), for three different values of contact angle (values of other relevant parameters are taken as $\bar{\omega} = 1$, $a = 2$, $\zeta_0 = -4$ and $\lambda = 0.2$). Please note that the term t_f refers to the capillary filling time. We have calculated the filling time t_f, which is the time taken by the central part of the interface to traverse a distance $L_1 = (x_2 - x_1) = (90 - 15)$ along the channel. The forward-backward motion of the capillary centerline is prominent for contact angles $\theta_s = 45^0$ and 135^0, whereas, the motion is relatively monotonic for the cases of $\theta_s = 90^0$. This is very interesting, since it implies that the receding of the interface occurs for favorable ($\theta_s = 45^0$) and non-favorable ($\theta_s = 135^0$) values of contact angles, whereas, it tends to decrease for a neutral contact angle ($\theta_s = 90^0$). Figure 8(b) depicts the position of the contact line with time (t_w), for the same set of variables taken in the previous figure (Fig. 8a). We first observe that the position of the contact line varies strongly as the contact angle is changed. Quite intuitively, the contact line traverses more distance when the

contact angle is favorable (i.e., $\theta_s = 45^0$) and less distance is covered in cases of unfavorable contact angle (i.e., $\theta_s = 135^0$). In tune with the previous figure, we again observe that for a neutral contact angle ($\theta_s = 90^0$) the deviation from a mean motion is the least, whereas, in the cases of favorable and non-favorable contact angles the deviation from a mean motion is larger, as indicated by the larger undulations in the x vs. t_f curve in the present figure.
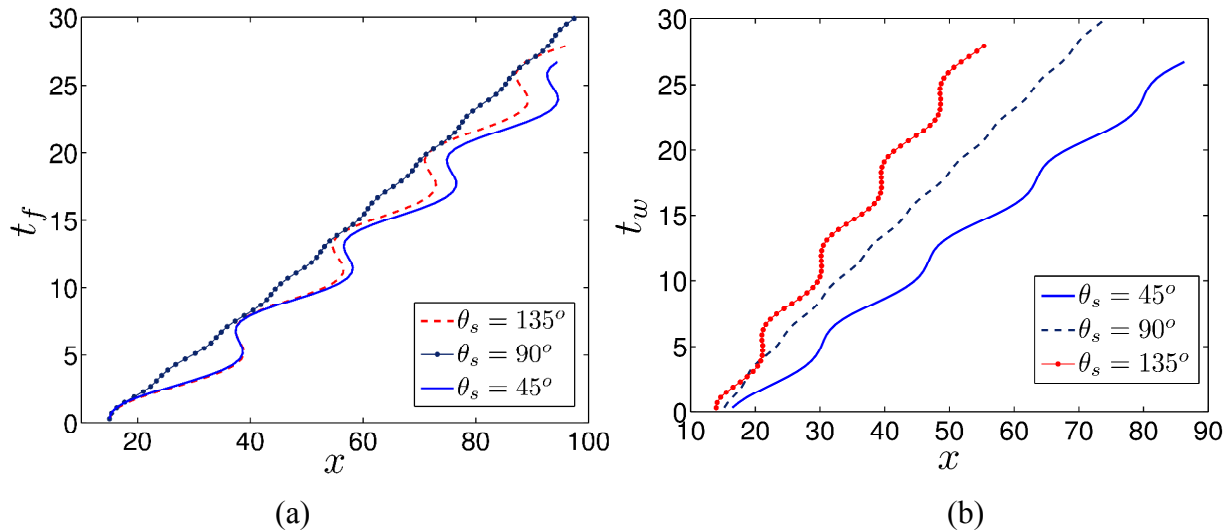

Fig. 8. (Color online) (a) Time (t_f) vs Capillary filling distance (x), for a =2.0 and $\bar{\omega}$=1. (b) Time (t_w) vs Capillary wetting distance (x) for a =2.0 and $\bar{\omega}$=1. For a given value of amplitude and frequency of the applied electric field, the increase in surface wettability decreases the wetting time and increases the filing time.

3.5. Scaling estimates for the filling time

We next move on to investigate whether the time taken by the advancing fluid to penetrate a certain distance into the capillary in a pulsating electric field driven environment obeys any generic scaling behavior for the given values of the fluid properties and the substrate wettability conditions. In order to do so, we display Fig. 9, which shows the variation of the length of the liquid column (x) as a function of time (t_f) for the different values of frequency and amplitude of the applied electric field. From Fig. 9, we attempt to quantify the appropriate scaling behavior of the filling time of advancing fluid into the capillary and find that the long time filling for all the cases considered approximately obeys a linear scaling: $x \sim t_f$.
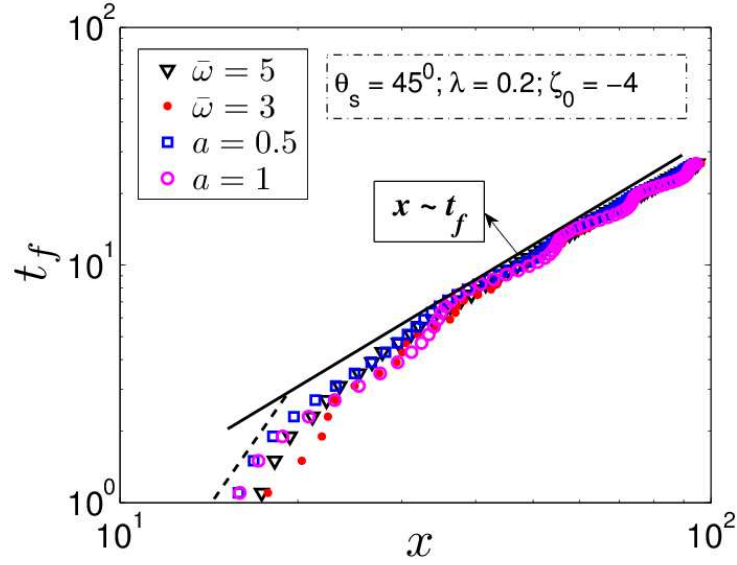
Fig. 9. (Color online) Filling time (t_f) vs. distance (x) for $\theta_s = 45^0$ for two different values of amplitude $a = 0.5$, 1 when $\bar{\omega} = 1$ and two different frequencies $\bar{\omega} = 3, 5$ when $a = 1$. The other parameters considered are: $\zeta_0 = -4, \lambda = 0.2$. The long time filling for all the cases exhibits a linear scaling x t_f.

3.6. Capillary filling power

We start our discussion on capillary filling power with figure 10(a), where we demonstrate the variation in the net power ($\tilde{P}$) with the axial location at two different times (*t*=50 and 100); other relevant parameters being mentioned in the caption. The interface locations at these times have also been shown in the figures. The most interesting thing to note from the present figures is that there is a dip in the ionic current at the location of the interface, which indicates that the interface creates a barrier for the ionic current to flow. Since we have taken into account the streaming current along with the conduction current, it is quite obvious that the flow field will strongly dictate the total current and hence the total power. Since near the interface some recirculation is observed and the axial velocity drops in both the fluids, the current along with it also drops, as evident from the present figure.
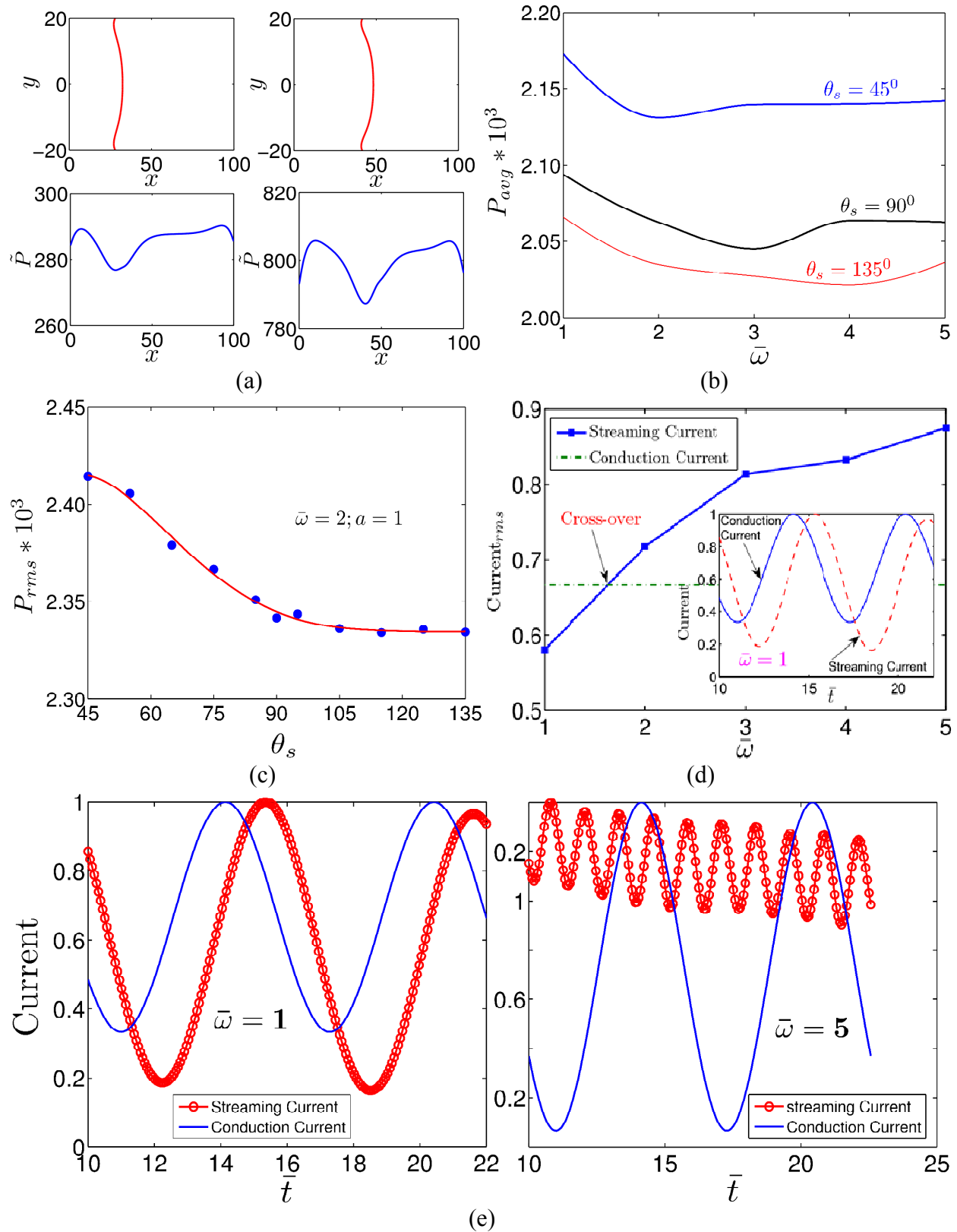
24

FIG. 10. (Color online) (a) Instantaneous net power ($\tilde{P}$) versus capillary filling distance (x), at two different times t=50 and 100, for $\theta_s = 45^0$, a =1.0 and $\bar{\omega}$ =1. (b) Capillary filling power (P_{avg})

versus frequency ($\bar{\omega}$), for a =1.0. (c) Capillary filling power (P_{rms}) versus static contact angle (θ_s), for a =1.0 and $\bar{\omega}$=2. (d) Currents (rms) normalized with its maximum value versus frequency ($\bar{\omega}$), for $\theta_s = 90^0$ and a =1.0. (e) Streaming and Conduction currents versus time ($\bar{t}$) for $\theta_s = 90^0$ and a =1.0 at two different frequencies: $\bar{\omega}$=1 and $\bar{\omega}$=5. The other parameters considered are: ζ_0 = -4 and λ = 0.2. A dip in the variation of instantaneous net power ($\tilde{P}$) is observed at the location of the interface separating two bulk phases. The variation of RMS power (P_{rms}) shows a decreasing trend with increasing surface wettability and becomes almost constant for hydrophobic surface ($\theta_s \geq 120^0$).There is a crossover on the variation of the currents (rms) at some frequency. A phase difference between the streaming current and the conduction current is observed and the phase difference increases with the increasing value of the frequency of the applied electric field.

Figure 10(b) depicts the variation in the average RMS power with the frequency of the external electric field for three different values of contact angles, $\theta_s = 45^0$, 90^0 and 135^0, while the other relevant parameters have been mentioned in the caption. We note from the present figure that there is a weak minimum for the averaged RMS power, the location of which shifts towards higher frequencies as the contact angle increases. However, a closer scrutiny of Fig. 10(b) clearly reveals that the average RMS power increases immediately after reaching the weak minimum value and finally, becomes constant even at higher frequencies for contact angle values $\theta_s = 45^0$ and 90^0. The reason behind such behavior can be attributed to the fact that as we increase the frequency, the forcing on the fluid changes direction very rapidly, as a result of which the velocity in the fluid is not able to develop fully, which brings down its magnitude. Therefore, at high frequencies, the dominant contribution on the current comes from the conduction current, which changes instantaneously with the applied electric field. Since the conduction current is independent of the forcing frequency, the power at high frequencies become almost independent of the forcing frequency as one can see from Fig. 10(d). We additionally note the fact that the velocity of the fluid and hence the streaming current are not in the same phase with the external electric field and this phase difference gets more prominent as the frequency is increased. We confirm this phenomenon in Fig. 10(e). The consequence of such a phase difference is that at certain frequencies, the streaming current is in the opposite direction of the conduction current as can be seen from Fig. 10(d), which brings down the total current and hence the total power. The minimum observed in the present figure is an outcome of such interactions between the conduction and the streaming current.

Figure 10(c) depicts the variation in the net RMS power with the contact angle; the remaining relevant parameters being mentioned in the caption. It can be observed from the present figure that the net power drops down as the contact angle is increased; however, it nearly becomes a constant at higher values of the contact angle. The decrease in the values of power is expected, since with increasing the contact angle, the interface and hence the displacing fluid (fluid A in the present study) witnesses more resistance to move forward, which in turn, decreases the velocity of the fluid. A decrease in the velocity naturally causes the streaming current to go down and hence a decrease in the resulting electrical power is observed. Since we have plotted the present figure for a frequency $\bar{\omega} = 2$, the relative or the percentage decrease in the total power is relatively small, owing to a diminished influence of the advective ion transport. The relative fall in the total power is thus expected to be higher for lower frequencies.

4. CONCLUSIONS

In the present study, we investigate the interfacial dynamics of contact line motion of two immiscible fluids driven by a time varying electric field through a microfluidic channel. We observe that the two important factors: the frequency and the amplitude of the time periodic electric field plays crucial role on the interfacial electro-hydrodynamics, which in turn alters the capillary filling dynamics appreciably. The most important findings from the present study can be summarized as follows:

i.   The variation of the frequency and amplitude of the applied pulsating electrical field alters the contact line velocity of two immiscible fluids as it moves over the solid surface having different wetting characteristics. Such alterations of contact line velocity, in effect, are achieved by the intricate interactions between the electrokinetic effects intrinsic to the AC electroosmotic flow of binary fluids and the surface tension effects as modulated by the alteration in the chemical characteristics of the channel substrate.

ii. Specific to $\theta_s = 45^0$, the contact line receding is observed for relatively lower value of frequency ($\bar{\omega} = 0.5$) and higher value   of amplitude (a=4), whereas for the higher frequencies and lower amplitudes, the receding phenomenon disappears completely. The alterations in contact line velocity (contact line receding) essentially culminate in altered capillary penetration rates.

27

iii. Unlike the case of $\theta_s = 45^0$, the contact line receding is also present for $\theta_s = 135^0$. However, in contrast with the receding phenomenon for $\theta_s = 45^0$, the contact line for $\theta_s = 135^0$ recedes at relatively higher frequencies and lower amplitudes. This is attributable to the imbalance in force acting over the interface arising due to the interfacial electro-chemical-hydrodynamics.

iv. We further observe that the two important parameters of time periodic electric field, namely, the frequency and the amplitude, do play significant roles towards altering the dynamics of capillary filling through narrow fluidic pathways. Either the decreasing value of frequency or the increasing value in the amplitude of the applied electric field allow the capillary to stop at some locations following acceleration-deceleration dynamics; this, in turn, speeds up the filling between some specified stations. Our results also reveal that the long time filling dynamics obeys a linear scaling.

v. We also make an effort to calculate the capillary filling power of binary fluid system into the channel where we show that the electric power required to fill the capillary strongly depends upon the external electric field and the ionic current generated in the flow field. In particular, we show that the frequency and the amplitude of the externally applied electric field alters the net power following the alteration in conduction current, whereas the surface wettability alters the streaming current following the alteration in flow velocity, which in turn alters the filling power appreciably.

Technological implications of the above inferences can be far-reaching. In fact, based on these observations, it may be inferred that the motion of the contact line in a practical scenario can be delicately controlled by tuning combinations of interfacial tension as modulated by the surface wettability and the time-periodic electrokinetic effects in a confined fluidic environment. Because of deployment of an alternating electric field, the contact line motion can be switched on and off at will, thereby improving the manueverity of capillary filling in lab-on-a-chip based microfluidic devices that are routinely employed for biochemical sample analysis. This opens up a new paradigm of micro-total-analysis systems that has remained unexplored by far.

REFERENCES

1. Y. D. Shikhmurzaev, *International Journal of Multiphase Flow*, 1993, **19**, 589–610.

2. Y. D. Shikhmurzaev, *Journal of Fluid Mechanics*, 1997, **334**, 211–249.

3. F. Mugele, *Soft Matter*, 2009, **5**, 3377.

4. R. Dey, K. Raj M, N. Bhandaru, R. Mukherjee, and S. Chakraborty, *Soft matter*, 2014, **10**, 3451–62.

5. C. L. Moraila-Martínez, M. A. Cabrerizo-Vílchez, and M. A. Rodríguez-Valverde, *Soft Matter*, 2013, **9**, 1664.

6. F.-C. Wang and H.-A. Wu, *Soft Matter*, 2013, **9**, 5703.

7. A. Askounis, D. Orejon, V. Koutsos, K. Sefiane, and M. E. R. Shanahan, *Soft Matter*, 2011, **7**, 4152.

8. Ľ. Fraštia, A. J. Archer, and U. Thiele, *Soft Matter*, 2012, **8**, 11363.

9. T. Kajiya, A. Daerr, T. Narita, L. Royon, F. Lequeux, and L. Limat, *Soft Matter*, 2013, **9**, 454.

10. G. Miquelard-Garnier, A. B. Croll, C. S. Davis, and A. J. Crosby, *Soft Matter*, 2010, **6**, 5789.

11. J. C. T. Eijkel and A. van den Berg, *Lab on a chip*, 2006, **6**, 1405–8.

12. J. Zhang and D. Y. Kwok, *Langmuir : the ACS journal of surfaces and colloids*, 2006, **22**, 4998–5004.

13. M. Hilpert, *Journal of colloid and interface science*, 2010, **347**, 315–23.

14. X.-P. Wang, T. Qian, and P. Sheng, *Journal of Fluid Mechanics*, 2008, **605**, 59.

15. T. Qian, X.-P. Wang, and P. Sheng, *Physical Review E*, 2003, **68**, 016306.

16.   A. Ashish Saha and S. K. Mitra, *Journal of colloid and interface science*, 2009, **339**, 461–80.

17.   J. Eggers and H. A. Stone, *Journal of Fluid Mechanics*, 2004, **505**, 309–321.

18.   D. Chakraborty, N. N. Dingari, and S. Chakraborty, *Langmuir*, 2012, **28**, 16701–10.

19.   M. O'Loughlin, C. Priest, M. N. Popescu, and J. Ralston, *Journal of colloid and interface science*, 2013, **402**, 259–66.

20.   R. Chebbi, *Journal of colloid and interface science*, 2011, **361**, 639–42.

21.   P. K. Mondal, U. Ghosh, A. Bandopadhyay, D. DasGupta, and S. Chakraborty, *Physical Review E*, 2013, **88**, 023022.

22.   D. J. C. M. 't Mannetje, F. Mugele, and D. van den Ende, *Langmuir : the ACS journal of surfaces and colloids*, 2013, **29**, 15116–21.

23.   W.-J. Luo, *Journal of colloid and interface science*, 2006, **295**, 551–61.

24.   J. Buehrle, S. Herminghaus, and F. Mugele, *Physical Review Letters*, 2003, **91**, 86101.

25.   A. Ramos, H. Morgan, N. G. Green, and A. Castellanos, *Journal of Physics D: Applied Physics*, 1998, **31**, 2338–2353.

26.   M.-H. Chang and G. M. Homsy, *Physics of Fluids*, 2005, **17**, 074107.

27.   D. Erickson, D. Sinton, and D. Li, *Lab on a chip*, 2003, **3**, 141–9.

28.   X. Luo, X.-P. Wang, T. Qian, and P. Sheng, *Solid State Communications*, 2006, **139**, 623–629.

29.   T. Qian, X.-P. Wang, and P. Sheng, *Journal of Fluid Mechanics*, 2006, **564**, 333.

30.   T. Qian, X.-P. Wang, and P. Sheng, *Physical Review Letters*, 2004, **93**, 094501.

31.   K. Luo, M.-P. Kuittu, C. Tong, S. Majaniemi, and T. Ala-Nissila, *The Journal of chemical physics*, 2005, **123**, 194702.

32.   W. Mickel, L. Joly, and T. Biben, *The Journal of chemical physics*, 2011, **134**, 094105.

33.   V. E. Badalassi, H. D. Ceniceros, and S. Banerjee, *Journal of Computational Physics*, 2003, **190**, 371–397.

34.   D. Borzacchiello, E. Leriche, B. Blottière, and J. Guillet, *Journal of Non-Newtonian Fluid Mechanics*, 2013, **200**, 52–64.

35.   H.-Y. Chen, D. Jasnow, and J. Viñals, *Physical Review Letters*, 2000, **85**, 1686–1689.

36.   D. Jacqmin, *Journal of Fluid Mechanics*, 2000, **402**, 57–88.

37.   P. Seppecher, *International Journal of Engineering Science*, 1996, **34**, 977–992.

38.   T. . Blake and J. . Haynes, *Journal of Colloid and Interface Science*, 1969, **30**, 421–423.

39.   L. Pismen and Y. Pomeau, *Physical Review E*, 2000, **62**, 2480–2492.

40.   J. W. Cahn and J. E. Hilliard, *The Journal of Chemical Physics*, 1958, **28**, 258.

41.   J. W. Cahn and J. E. Hilliard, *The Journal of Chemical Physics*, 1959, **31**, 688.

42.   H. Ding and P. Spelt, *Physical Review E*, 2007, **75**, 046708.

43.   J. H. Masliyah and S. Bhattacharjee, *Electrokinetic and Colloid Transport Phenomena*, Wiley, 2006.

44.   R. Hunter, *Zeta potential in colloid science : principles and applications*, Academic Press, London ;New York, 1981.

45.   Y. Lin, P. Skjetne, and A. Carlson, *International Journal of Multiphase Flow*, 2012, **45**, 1–11.

46.   S. Das and S. Chakraborty, *Analytica Chimica Acta*, 2006, **559**, 15–24.

47.   A. M. Afonso, M. A. Alves, and F. T. Pinho, *Journal of colloid and interface science*, 2013, **395**, 277–86.

48.   S. S. Bahga, O. I. Vinogradova, and M. Z. Bazant, *Journal of Fluid Mechanics*, 2010, **644**, 245.

49.   W. Saslow, *Physical Review E*, 2003, **68**, 051502.

50.   M. Bazant, K. Thornton, and A. Ajdari, *Physical Review E*, 2004, **70**, 21506.

51.   L. Højgaard Olesen, M. Z. Bazant, and H. Bruus, *Physical Review E*, 2010, **82**, 011501.

52.   W. C. Chew and P. N. Sen, *The Journal of Chemical Physics*, 1982, **77**, 4683.